

Reconstructing phase space of injection beam based on the measurement of accumulated beam: A novel tomography algorithm and its applications

H. Y. Liu^{1,2}, S. Y. Xu^{1,2,3}, M. T. Li^{1,2}, Y. S. Yuan^{1,2,3},
L. S. Huang^{1,2}, X. Y. Feng^{1,2,3} and S. Wang^{1,2,3,*}

¹*Institute of High Energy Physics, Chinese Academy of Sciences, Beijing 100049, China*

²*Spallation Neutron Source Science Center, Dongguan 523803, China*

³*University of Chinese Academy of Sciences, Beijing 100049, China*



(Received 10 October 2023; accepted 18 April 2024; published 21 May 2024)

The measurement of phase space has always been an important topic in the field of accelerator physics, playing an indispensable role in understanding the beam dynamics. The phase space distribution of the injected beam is crucial for optimizing the multiturn accumulation injection process in synchrotrons. However, directly and accurately measuring the phase space distribution is a challenging task. In this study, we propose an innovative tomographic algorithm based on the measurement data of the accumulated beam profile obtained from the wall current monitor (WCM) in a synchrotron, to reconstruct the longitudinal phase space of the injected beam. Simulations were conducted for various initial distribution scenarios, and the results showed that this algorithm can achieve a difference of about 4% in the rms momentum spread between the initial and reconstructed phase space distribution of the injected beam. This algorithm has been applied to the China Spallation Neutron Source and successfully measured the momentum spread of the injected beam. Machine studies considering the phase error of the injected beam showed a high consistency between the reconstructed beam profiles and the measurement results from the WCM on Rapid Cycling Synchrotron. The research results demonstrate that this algorithm can be an effective approach for measuring the momentum distribution of the injected beam in a synchrotron. Furthermore, this method also has the potential to be extended to reconstruct the transverse phase space of the injected beam.

DOI: [10.1103/PhysRevAccelBeams.27.052804](https://doi.org/10.1103/PhysRevAccelBeams.27.052804)

I. INTRODUCTION

The measurement of phase space has always been a crucial topic in the field of accelerator beam dynamics, and tomography is one of the most commonly used methods for achieving phase space measurements [1–7]. Typically, tomography is based on beam profile data obtained at different positions or under different conditions, and the phase space distribution can be reconstructed through iterative processes. The phase space distribution of the injected beam is one of the key parameters and plays an important role in optimizing the multiturn accumulation injection process [7–10]. In this paper, a new tomographic imaging algorithm is proposed to obtain the phase space distribution of the injected beam by utilizing profile measurement data accumulated from multiple turns of injected beams. This method is applicable to various beam

profile measurement instruments, such as wall current monitors (WCM), fast current transformers (FCT), strip cameras, beam shape monitors, ionization profile monitors (IPMs), and other relevant devices.

To provide a more specific introduction to this algorithm, we will take the measurement of the momentum spread of an injected beam in a synchrotron as an example, which is of great significance for longitudinal injection, multiturn injection, and beam dynamics research in synchrotron [11–15]. Traditional measurement methods typically involve measuring the envelope growth caused by the dispersion effect of bending magnets in linac [16]. However, this method can be only applicable when the beta function is much smaller than the dispersion function and is commonly used in electron accelerators. In proton linear accelerators, on the other hand, it is often necessary to fit the beam's energy spread by measuring variations in the beam's length [15], which places higher demands on the precision and quantity of the measurement components. Our algorithm mainly reconstructs the initial longitudinal phase space of the injected beam based on the profile data of accumulated beams from the WCM in the synchrotron. Compared with the traditional tomography that reconstructs based on the longitudinal beam profile of a single-turn injected beam, this algorithm reduces the requirement for WCM's resolution.

*wangs@ihep.ac.cn

Published by the American Physical Society under the terms of the *Creative Commons Attribution 4.0 International* license. Further distribution of this work must maintain attribution to the author(s) and the published article's title, journal citation, and DOI.

TABLE I. Main parameters of the CSNS RCS.

Parameters (unit)	Value
Circumference (m)	227.92
Harmonic number	2
Repetition rate (Hz)	25
Accelerating period (ms)	20
Injection kinetic energy spread (%)	± 0.05
Injection fundamental rf frequency (MHz)	1.022
Extraction fundamental rf frequency (MHz)	2.444
Number of particles per bunch	7.8×10^{12}
Beam power on target (kW)	100
Injection kinetic energy (GeV)	0.08
Extraction kinetic energy (GeV)	1.6
Transition gamma	4.89
Chopper duty	0.5

This algorithm is used on the China Spallation Neutron Source (CSNS), whose accelerator part consists of an 80 MeV negative hydrogen linear accelerator and a 1.6 GeV Rapid Cycling Synchrotron (RCS) with a harmonic number of 2, the main parameters of CSNS RCS are listed in Table I. CSNS RCS is a high-intensity proton accelerator, with a design beam power of 100 kW [17] and has been operating at 140 kW since October 2022. Figure 1 shows the linac time structure corresponding to 100 kW of CSNS. The linac rf frequency is 324 MHz, and the length of each micropulse is 3 ns. It is injected into RCS using a multiturn painting method, with two bunches injected per turn. When the chopping duty is 50%, the length of the bunch and gap is 489 ns, that is, each bunch consists of 159 micropulses. The number of injection turns is about 200, and the corresponding pulse length of the beam is 391 μm . To reduce the beam loss caused by the transverse space charge effect, CSNS RCS adopts the longitudinal painting method to lower the longitudinal charge line density [18]. And to control the longitudinal distribution in RCS more accurately, the measurement of the longitudinal phase space distribution of the injected beam is essential, which is also the original intention of developing

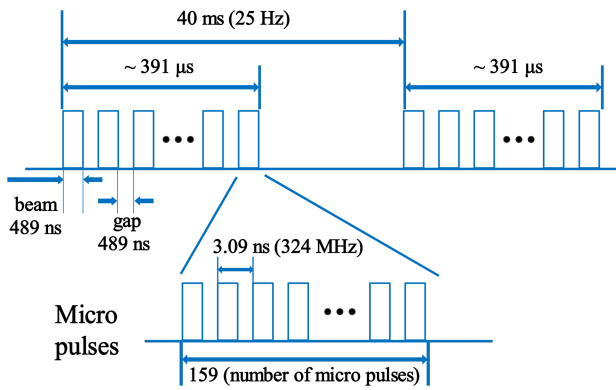


FIG. 1. Time structure of the linac beam pulse.

this algorithm. The main beam measurement diagnostics devices used in the experiment include FCT and WCM. The FCT on the Linac to Ring Beam Transport (LRBT) measures the energy using the time-of-flight method, while the WCM on the LRBT is used to measure the longitudinal distribution of the injected beam. And the WCM on the RCS is used to provide the longitudinal distribution of the accumulated beam, which is also the primary input data for the algorithm.

In this paper, we developed a new method based on tomography algorithm to measure the initial phase space distribution of the beam with the accumulated beam profile data in a synchrotron. This approach ensures the reconstruction of the injection beam's phase space distribution even when using accumulated beam profile data with lower measurement device precision. This paper is organized as follows: Sec. I is the introduction; Sec. II introduces the structure of our algorithm, the related simulation results, and the influence of injection phase error; Sec. III introduces the application of the algorithm to CSNS RCS; and Sec. IV is the conclusion.

II. PHASE SPACE RECONSTRUCTION ALGORITHM

A. Introduction of algorithm

This algorithm is based on the algebraic reconstruction technique (ART) [5] and involves multiple-turn accumulation of the initially assumed beam phase space distribution, comparison with the accumulated beam profile data, and iterative error correction. The errors between the assumed initial beam distribution and the measured accumulated beam profiles are backpropagated to refine the initial assumption, ultimately yielding the reconstructed longitudinal phase space distribution of the injected beam. Like other ART algorithms, this algorithm also employs a mapping for simulating the longitudinal dynamics of the multiturn injection process. For further details, please refer to Appendix A.

Figure 2 illustrates the reconstruction algorithm. First, a phase space distribution is generated, and then the longitudinal phase space distribution after injection is obtained by tracking and superimposing the multiturn injected bunches. By continuing the tracking calculation, the beam shape can be obtained at different sampling turns. To facilitate the evaluation of the discrepancy between the reconstructed and the measured beam profiles, we define a similarity factor R_n as shown in the following equation:

$$R_n = 1 - \frac{\sum_{\text{bins}} (N_{m,i} - N_{g,i})^2}{N_{\text{total}}^2},$$

where R_n is the similarity factor, $N_{m,i}$ represents the measured particle number of the i th data point, $N_{g,i}$ represents the reconstructed particle number of the i th data

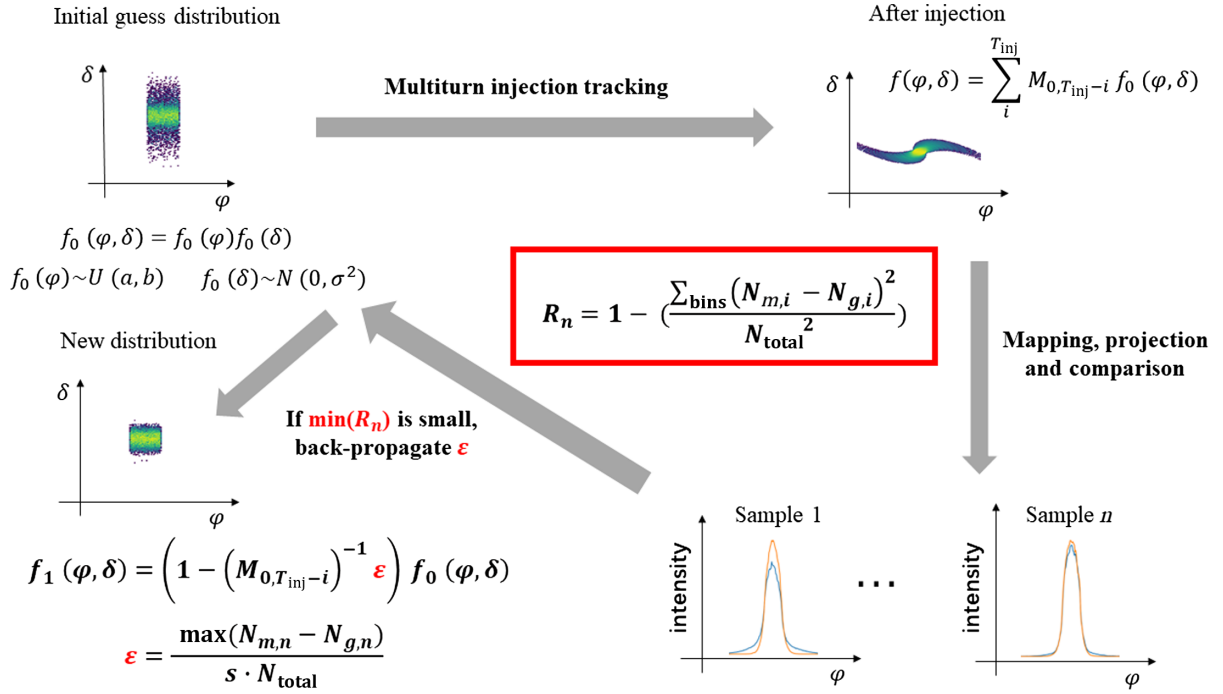


FIG. 2. Demonstration diagram of tomography algorithm. First, a phase space distribution f_0 is generated with a uniform distribution in the phase direction and a Gaussian distribution in the momentum direction. Then the longitudinal phase space distribution after injection is obtained by tracking and superimposing the multiturn injection bunches, in which $M_{0, T_{inj}-i}$ is the longitudinal mapping from 0 to $T_{inj}-i$ turn. By continuing the tracking calculation, the beam shape can be obtained in different sampling turns. Here $N_{m,i}$ represents the measured particle number of the i th data point within the bins, $N_{g,i}$ represents the reconstructed particle number of the i th data point within the bins and N_{total} represents the total particle number. The gap between the reconstructed value and the measured value, denoted as R_n , is calculated and used as a convergence criterion. If the minimum value of R_n does not meet the given requirement, the maximum error value ϵ is scaled back to the initial distribution by a factor denoted as s . The iterative process continues until the convergence criterion is met.

point, and N_{total} represents the total particle number. This similarity factor can be used to quantify the closeness between the reconstructed beam and the actual measured values. A value closer to 1 indicates a higher similarity between the reconstruction and the measurement. If the minimum value of R_n does not meet the given requirement, the maximum error value is iteratively backpropagated to the initial distribution in a certain proportion. This iterative process is repeated until the convergence criterion is satisfied.

B. Simulation results and phase error analysis

Our algorithm is presented using a simulation example of measuring the injected beam's momentum spread in CSNS RCS. To better reflect the real situation, some considerations need to be taken into account when applying the algorithm. First, in the most proton synchrotrons, the longitudinal beam size is much larger than the transverse beam size, so the longitudinal motion process can be considered separately. Therefore, the mapping process only considers the phase and the momentum spread. Second, due to the low accuracy of linac energy measurement, the beam injected into RCS may have a momentum offset, so

the algorithm itself needs to be able to restore this process. In addition, the accurate injection phase of CSNS RCS cannot be measured, so it is necessary to analyze the effect of the injection phase error on the algorithm.

The objective is to determine the distribution of an 80.3 MeV beam based on a predefined structure in 2D longitudinal phase space. The structure consists of a uniform distribution in the phase direction and a Gaussian distribution in the momentum direction. An 80% chopper duty was used, which means that the initial bunch length in the phase direction is approximately 36° . As a result, each bunch injected into the RCS is composed of 64 microbunches, with the RCS rf frequency starting point being approximately 1.022 MHz. The distribution function is denoted by $f_0(\phi, \delta)$, and we assume that each bunch of the multiturn injected beam is identical, and the longitudinal phase distribution is always uniform and constant in length according to this time structure. The initial distribution in the momentum direction is given by a single-peak Gaussian distribution. To improve the clarity of the WCM signal after injection completion, the number of injection turns is set to 25. The longitudinal profile data of the beam, obtained for phase space reconstruction, are collected after the injection.

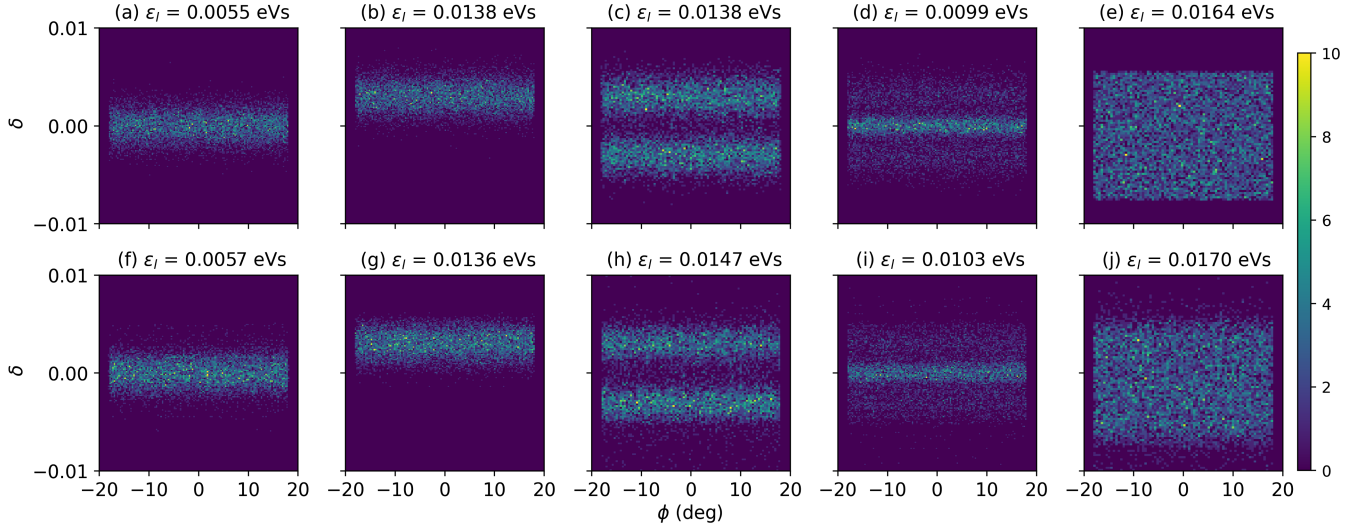


FIG. 3. Comparisons between the simulation and reconstructed phase space with our algorithm. (a)–(e) are the assumed initial distribution under different scenarios, while (f)–(j) show the corresponding reconstruction results obtained using the proposed method.

The sampling range spans 60 turns, comprising 10 sets of data, which correspond to approximately 180° of longitudinal phase space rotation. Due to the low intensity in measurement, the mapping process utilizes the longitudinal motion equation without considering the longitudinal space charge effects [18,19]. It is worth noting that in our application scenario, the uniform distribution and beam length (from 100 to 500 ns) can be inferred from the longitudinal structure of the linac beam pulse, as depicted in Fig. 1, along with the chopper duty. Therefore, the initial beam profile is always known. This serves as the basis for using the algorithm to measure the momentum spread from the linac. Since its distributions in the phase and momentum spread directions can be considered separately, the cumulative probability density distribution function in the momentum direction is calculated independently after each iteration. Based on this distribution, an equivalent number of particles is generated and combined with the phase of particles to form phase space coordinates, which ensures the 2D phase space uncorrelated in the subsequent iterations.

As shown in the upper part of Fig. 3, the different initial distributions are provided as simulation results. From Figs. 3(a)–3(e), they are, respectively, a single-peak Gaussian distribution, a Gaussian distribution with momentum offset, a double-peak Gaussian distribution, a triple-peak Gaussian distribution, and a uniform distribution. The corresponding reconstructed images for each initial distribution are shown in Figs. 3(f)–3(j), and their minimum similarity factors have all exceeded 99%. Table II presents the rms values of the simulated (Sim.) and reconstructed (Rec.) momentum distributions in Fig. 3. It can be observed that the simulated and reconstructed values are very close for different distributions. Apart from the double-peak Gaussian distribution, the different values (Dif.) are less than 4%, which also proves the accuracy of the algorithm.

To demonstrate the generality of our method, we have included in Appendix B the algorithm validation results under different assumed longitudinal initial distributions. However, given the practical constraints of our accelerator in generating beams with other longitudinal distributions, these results are unable to be experimentally measured and applied. Consequently, the main text continues to focus on the assumption of uniform distribution.

However, the phase of the beam cannot be precisely determined though beam diagnostics elements when the beam enters the synchrotron. Additionally, due to the weak intensity of the single-pulse beam, the beam diagnostics elements within the synchrotron are also unable to detect the accurate phase of the beam. Therefore, when we have the given initial beam distribution from the linac, we need to consider the impact of phase errors on the accuracy of the reconstruction process. Based on the five distributions provided in Fig. 3, we analyzed the impact of different phase error values on the minimum similarity factor, as shown in Fig. 4. It is evident that the phase error has a significant impact on the similarity factor. Taking the Gaussian distribution as an example, with a phase error of 10° , the minimum similarity factor decreases to below 80%. Although different distributions are affected differently by

TABLE II. Comparison on the rms value of the simulated and reconstructed momentum in five different initial distributions.

Initial distribution	Sim. (%)	Rec. (%)	Dif. (%)
(a), (f)	0.130	0.134	2.99
(b), (g)	0.328	0.323	1.52
(c), (h)	0.328	0.350	6.28
(d), (i)	0.237	0.243	2.47
(e), (j)	0.388	0.403	3.72

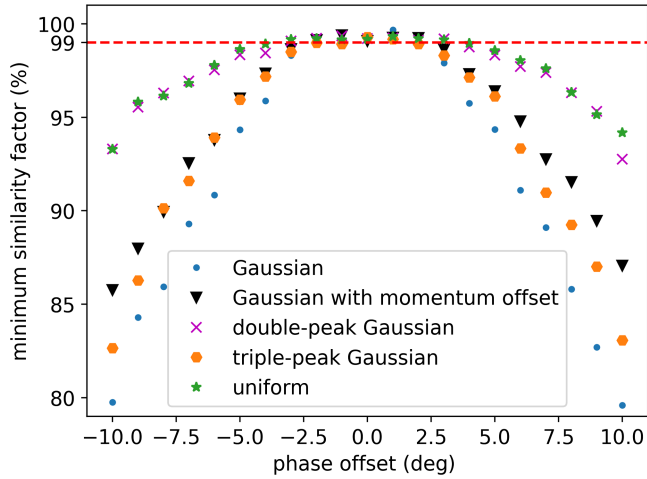


FIG. 4. Influence of different phase errors on similarity calculation.

phase errors, all of them can maintain a minimum similarity factor of 99% or higher when the phase error is within $\pm 3^\circ$.

After considering the phase error in the initial distribution, the minimum similarity factor can still be higher than 99%. Therefore, in the experiment, we scan the initial phase of the injected beam with a step size of 3° to minimize the impact of phase errors.

III. MEASUREMENT RESULT

Next, we take the CSNS RCS as an application example to demonstrate the performance of this algorithm in the experiment and highlight the considerations needed during its implementation. It employs a multiturn H^- stripping injection method. In the experiment, we scanned the chopper phase under the larger bunch lengths of the injected beam to reduce the beam loss during the rf capture process and used this as a criterion to determine the injection phase. This approach was chosen because, in

the long bunch length mode, when the beam loss in the dispersion section and the longitudinal emittance are at their lowest, the injection phase closely approximates the 0° phase of the rf bucket. The rf voltages are also calibrated by using the synchronous oscillation frequency of the measured data. Furthermore, the timing signal discrepancies are corrected by comparing the difference in the peak turns between the measured data and the reconstructed data. As shown in Fig. 5, the results of one experimental reconstruction are presented. Figure 5(a) represents the longitudinal phase space of the beam from the linac, and Fig. 5(b) shows the comparison between the WCM data from different turns on the RCS and the corresponding reconstructed values. During the experiment, a total of 25 turns of the beam were injected, with each turn having a bunch length of 35.5° . The rf frequency of the RCS during the experiment was 1.02379 MHz, corresponding to a synchronous particle energy of 80.3 MeV, and the cavity voltage was approximately 46 kV. For the reconstruction, a total of 10 sets of sampling data were used, spanning 54 turns, with the longitudinal oscillation period being 114 turns, which corresponds to approximately 170° of the longitudinal phase space rotation. From (b), it can be observed that the reconstructed data closely match the WCM data, with a similarity factor maintained above 96.9%. The decrease in the similarity factor compared to the 99% observed in the simulation could be mainly attributed to errors in the initial beam length estimation and inaccuracies in the WCM data. In this algorithm, the convergence criterion is based on minimizing the maximum error, or equivalently, maximizing the similarity factor. As a result, during the iterative process, the reconstruction prioritizes reducing the error associated with the turns that have higher peak current densities, such as turns 59, 65, and 71 in Fig. 5(b), where the similarity factor is particularly sensitive. This leads to a smoother reconstructed distribution when the peak current density is high. However, this approach may also result in less accurate matching of the top details for other turns [for example, turns 41, 47, and 89 in

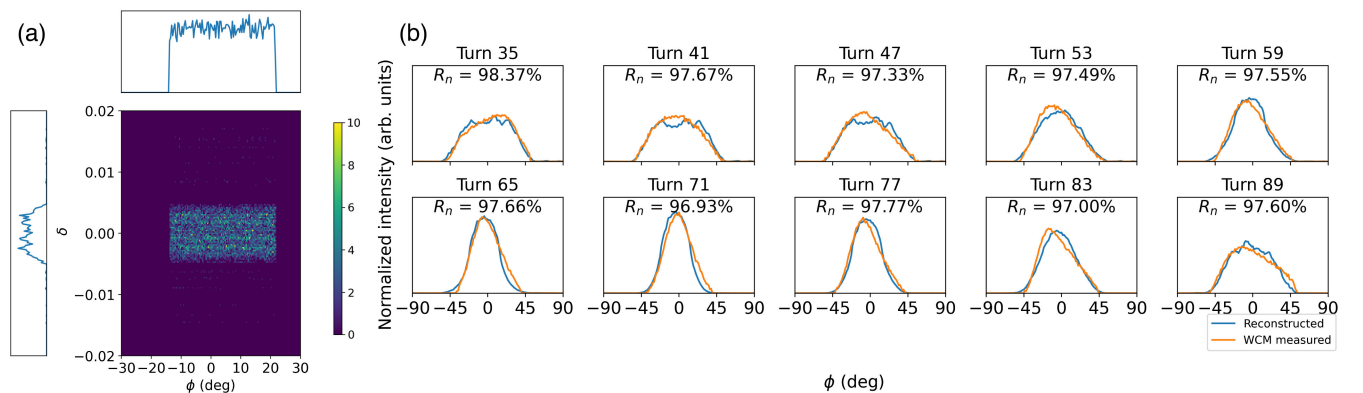


FIG. 5. Reconstruction results from experimental measurements at CSNS RCS are presented as follows: (a) reconstructed phase space distribution. (b) Comparisons between the reconstructed and measured bunch shape in different turns.

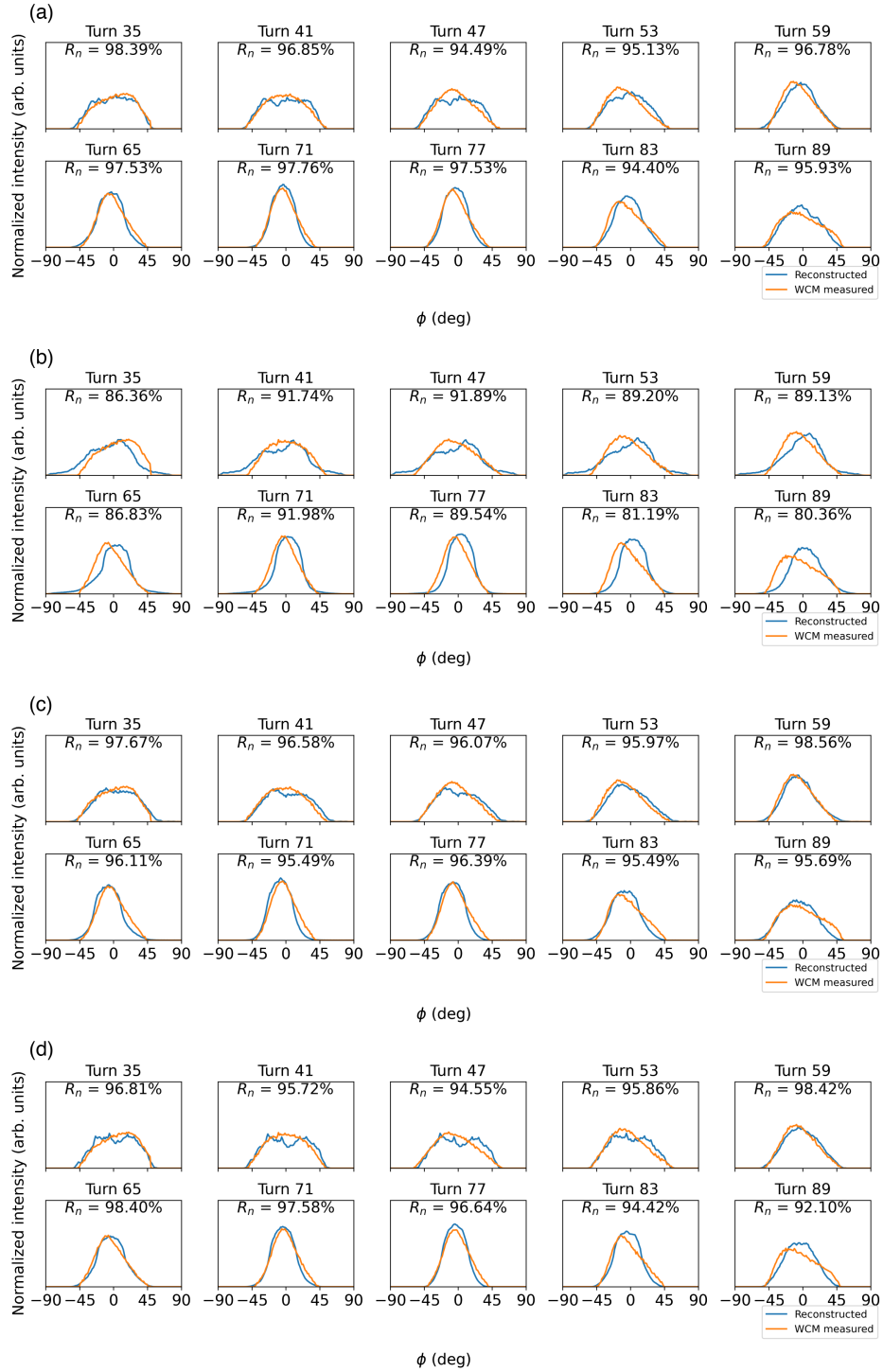


FIG. 6. Comparisons between the reconstructed and measured bunch shape were conducted under different conditions and turns. Specifically, the chopper phase during measurement was set to -6° in (a), $+6^\circ$ in (b), -6° with the initial phase optimized in (c), and $+6^\circ$ with the initial phase optimized in (d).

Fig. 5(b)]. Given that the intended application of this algorithm is for scenarios where the WCM resolution is inherently low, it is reasonable to prioritize data with higher peak current densities as they are more reliable.

The measured $\Delta p/p$ rms value in Fig. 5 is approximately 0.276%, which falls within the permissible level of the design value. And the longitudinal emittance is 0.0128 eVs, which falls within the same range as the

emittance provided in Fig. 3. Therefore, the measured values are within the validation range of the algorithm. Due to the current lack of beam diagnostic elements in the linac, there is no capability for cross comparison of this measurement result. However, with the advancement of the CSNS upgrade plan (CSNS-II), there is a plan of evaluating the measurement accuracy of the algorithm through other measurement methods in the future.

We also studied the influence of phase errors on the similarity in the machine study. Figure 6 shows the comparison between the reconstructed and measured longitudinal distributions under different phase errors. In Figs. 6(a) and 6(b), there are -6° and $+6^\circ$ of chopper phase difference compared to Fig. 5. It can be seen that with large phase errors, the similarity also decreases significantly, which is consistent with the simulation results in Fig. 4. Figures 6(c) and 6(d) show the results obtained after optimizing the injection phase in the initial assumption. By comparing with (a) and (b), it can be seen that the error between the reconstructed and measured distributions is significantly improved. The similarity factor for the -6° phase increases from 94.4% to 95.49%, while for the $+6^\circ$ phase, it increases from 80.36% to 92.1%.

Under ideal conditions, a phase error introduced from either side (-6° or $+6^\circ$) should result in symmetrical effects, akin to the pattern in Fig. 4, where phase variations symmetrically affect the minimum similarity factor, with both positive and negative phase errors having equivalent impacts. However, symmetry is not consistently achieved due to longitudinal oscillations and the possibility that the optimal injection phase is nonzero, leading to a notable difference in the minimum similarity factor in Figs. 6(a) and 6(b). Other factors can also influence this process, such as WCM errors, timing errors, and inaccuracies in the mapping during measurement. These contribute to the challenge of achieving an exact injection phase correction, leading to ongoing differences even after optimization efforts, as depicted in Figs. 6(c) and 6(d). However, comparing the optimized phase [Figs. 6(c) and 6(d)] with the unoptimized [Figs. 6(a) and 6(b)], it is evident that the overall similarity is significantly improved after optimization. Nevertheless, the importance of phase correction cannot be overstated, as it is a key to preserve a high similarity factor. This process is critical for maintaining the measurement result of momentum spread within a margin of error that is acceptable, thereby ensuring the accuracy and dependability of beam diagnostics.

Although the similarity factor improved greatly after optimizing the injection phase, there is still a certain gap compared to the best injection phase found in the measurement. To compare the impact of this similarity factor difference on the measurement results, we compare the momentum spread distributions obtained under three different chopper phase settings, as shown in Fig. 7. It can be seen that the maximum momentum spread is consistent in

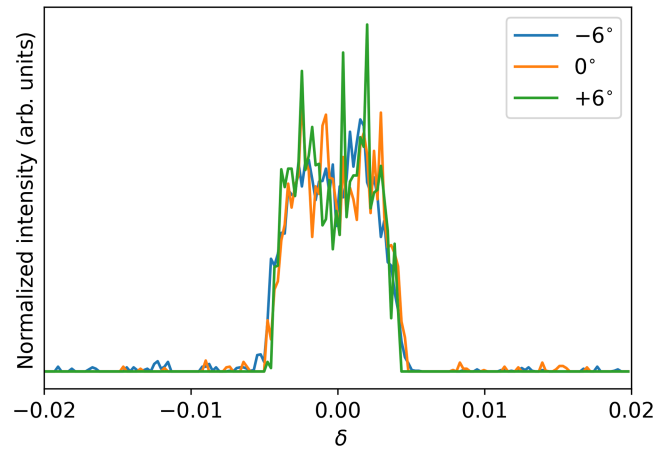


FIG. 7. Comparisons between the reconstructed initial momentum distribution under different chopper phases.

all three cases, around 0.5%. However, their distributions are quite different, which is reflected in the rms values. The rms values for -6° , 0° , and 6° are 0.2953%, 0.276%, and 0.2323%, respectively, which is a 15.83% difference. This result shows that the algorithm has a strong robustness to phase errors when measuring the maximum momentum spread, but it requires that the measured bunch can be well located at the bucket center to improve the accuracy of the measured distribution results.

IV. CONCLUSION

In summary, we have presented a new tomography algorithm based on the WCM data of accumulated beam to measure the phase space distribution of the injected beam. With this method, the longitudinal phase space distribution can be reconstructed even when the precision of longitudinal distribution measurement elements is relatively low. By defining the similarity factor, we can evaluate the accuracy of the reconstructed results and analyze the influence of phase error on the measurement results based on this. Simulation results indicate that the difference values of the rms momentum spread between the reconstructed and initial phase space distributions of the injected beam using this algorithm can achieve about 4%. The results demonstrate the feasibility of the algorithm for measuring the momentum spread of the injected beam. This algorithm solves the problem of the lack of effective measurement of longitudinal initial distribution in CSNS RCS and can also better integrate measurement results with simulation results, promoting further research on longitudinal behavior in synchrotron. This method is not limited to longitudinal applications. By appropriately adjusting the assumptions related to the initial beam distribution, mapping process, and iterative errors, this algorithm can also be applied to measure the transverse phase space of the injected beam, thus enabling the reconstruction of the

six-dimensional phase space distribution of the injected beam in a synchrotron. In the future, by combining the use of IPM on the CSNS RCS, it is expected to reconstruct the transverse phase space distribution of the injected beam. We hope this could provide crucial insights for the study of injection painting.

ACKNOWLEDGMENTS

This work is supported by the National Natural Science Foundation of China (Grant No. 12075134) and the Guangdong Basic and Applied Basic Research Foundation (Grant No. 2021B1515120021). This work is also partly supported by the Guangdong Basic and Applied Basic Research Foundation (Project No. 2024A1515012658) and the International Partnership Program of Chinese Academy of Sciences (Project No. 013GJHZ2023026FN).

APPENDIX A: LONGITUDINAL MAPPING

For a synchrotron with an rf cavity, the one-turn difference equation can be defined as follows:

$$\delta_{n+1} = \delta_n + \frac{eV}{\beta^2 E} [\sin(\phi_n) - \sin(\phi_s)],$$

$$\phi_{n+1} = \phi_n + 2\pi h \eta \delta_{n+1},$$

where e is the unit of charge, V is the rf voltage amplitude, β and E are the relativistic velocity factor and the energy of the synchronous particle, respectively, ϕ_s is the synchronous phase, h is the harmonic number, and η is the phase slip factor.

As depicted in Fig. 2, the longitudinal transfer matrix $M_{0,n}$ from the 0th to the n th turn is derived from the above equations. Both in reconstruction and simulation, we adopt the particle-in-cell concept, initially generating approximately 200 000 macroparticles. Then, the density distribution of these macroparticles across the phase space grid points (256×256 in this study) is determined and processed iteratively.

APPENDIX B: COMPARATIVE SIMULATION ANALYSIS: GAUSSIAN AND GAMMA DISTRIBUTIONS

As illustrated in the upper portion of Fig. 8, various initial distributions are presented as outcomes of the simulation. Specifically, Figs. 8(a) and 8(e) depict scenarios with a Gamma distribution in the phase direction and a Gaussian distribution in the momentum spread direction. Figures 8(b) and 8(f) showcase a Gamma distribution in the phase direction coupled with a uniform distribution in the momentum spread direction. Additionally, Figs. 8(c) and 8(g) represent instances where both the phase direction and momentum spread direction exhibit a Gaussian distribution. Finally, Figs. 8(d) and 8(h) display phase space with a Gaussian phase distribution and a uniform momentum spread distribution.

Table III displays the rms values for both the simulated (Sim.) and reconstructed (Rec.) momentum distributions as depicted in Fig. 8. A comparison reveals that the simulated and reconstructed values are highly consistent across various distributions. The differences between these values, indicated as ‘‘Dif.’’ in this table, are minimal, with a discrepancy of less than 4%. This level of accuracy is

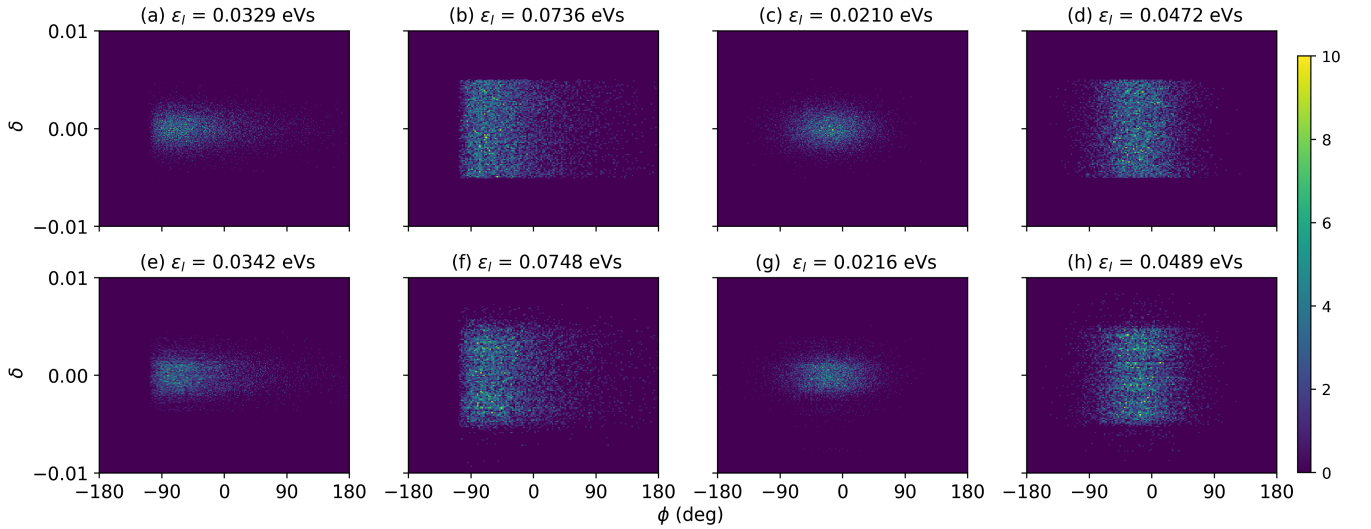


FIG. 8. Comparisons between the simulation and reconstructed phase space with our algorithm. (a)–(d) are the assumed initial distribution under different scenarios, while (e)–(h) show the corresponding reconstruction results obtained using the proposed method.

TABLE III. Comparison on the rms value of the simulated and reconstructed momentum in four different initial distributions.

Initial distribution	Sim. (%)	Rec. (%)	Dif. (%)
(a), (e)	0.129	0.133	3.10
(b), (f)	0.288	0.296	2.78
(c), (g)	0.129	0.131	1.55
(d), (h)	0.287	0.298	3.69

consistent with what was observed for the uniform phase distribution.

-
- [1] A. C. Kak and M. Slaney, *Principles of Computerized Tomographic Imaging* (SIAM, Philadelphia, PA, 2001).
- [2] R. Roussel, A. Edelen, C. Mayes, D. Ratner, J. P. Gonzalez-Aguilera, S. Kim, E. Wisniewski, and J. Power, Phase space reconstruction from accelerator beam measurements using neural networks and differentiable simulations, *Phys. Rev. Lett.* **130**, 145001 (2023).
- [3] V. Yakimenko, M. Babzien, I. Ben-Zvi, R. Malone, and X.-J. Wang, Electron beam phase-space measurement using a high-precision tomography technique, *Phys. Rev. ST Accel. Beams* **6**, 122801 (2003).
- [4] D. Stratakis, R. A. Kishek, H. Li, S. Bernal, M. Walter, B. Quinn, M. Reiser, and P. G. O'Shea, Tomography as a diagnostic tool for phase space mapping of intense particle beams, *Phys. Rev. ST Accel. Beams* **9**, 112801 (2006).
- [5] S. Hancock, M. Lindroos, and S. Koscielniak, Longitudinal phase space tomography with space charge, *Phys. Rev. ST Accel. Beams* **3**, 124202 (2000).
- [6] J. J. Scheins, Tomographic reconstruction of transverse and longitudinal phase space distribution using the maximum entropy algorithm, TESLA Report 2004-08, 2004.
- [7] M. Yoshimoto *et al.*, Measurement of momentum spread of the injection beam with longitudinal tomography method in the J-PARC RCS, in *Proceedings of the 6th International Particle Accelerator Conference, IPAC-2015, Richmond, VA (JACoW, Geneva, Switzerland, 2015)*.
- [8] H. Liu and S. Wang, Longitudinal beam dynamic design of 500 kW beam power upgrade for CSNS-II RCS, *Radiat. Detect. Technol. Methods* **6**, 339 (2022).
- [9] H. Hotchi *et al.*, Achievement of a low-loss 1-MW beam operation in the 3-GeV rapid cycling synchrotron of the Japan Proton Accelerator Research Complex, *Phys. Rev. Accel. Beams* **20**, 060402 (2017).
- [10] M. Y. Huang, Y. Irie, S. Y. Xu, X. Qi, and S. Wang, Performance of the correlated painting based on the mechanical structure of the anticorrelated painting scheme, *Phys. Rev. Accel. Beams* **25**, 110401 (2022).
- [11] H. Hotchi *et al.*, Beam commissioning of the 3-GeV rapid cycling synchrotron of the Japan Proton Accelerator Research Complex, *Phys. Rev. ST Accel. Beams* **12**, 040402 (2009).
- [12] S. Henderson *et al.*, The Spallation Neutron Source accelerator system design, *Nucl. Instrum. Methods Phys. Res., Sect. A* **763**, 610 (2014).
- [13] B. Cathey, S. Cousineau, A. Aleksandrov, and A. Zhukov, First six dimensional phase space measurement of an accelerator beam, *Phys. Rev. Lett.* **121**, 064804 (2018).
- [14] C. Sun, J. Li, G. Rusev, A. Tonchev, and Y. Wu, Energy and energy spread measurements of an electron beam by Compton scattering method, *Phys. Rev. ST Accel. Beams* **12**, 062801 (2009).
- [15] C. M. Bhat, Energy spread measurements for 400 MeV Linac beam at Fermilab Booster using a laser notcher system, Fermi National Accelerator Laboratory, Batavia, IL, Technical Report, No. FERMILAB-CONF-19-452-AD, 2019, <https://lss.fnal.gov/archive/2019/conf/fermilab-conf-19-452-ad.pdf>.
- [16] T. Suwada, M. Satoh, and K. Furukawa, Nondestructive beam energy-spread monitor using multi-strip-line electrodes, *Phys. Rev. ST Accel. Beams* **6**, 032801 (2003).
- [17] S. Xu *et al.*, Beam commissioning and beam loss control for CSNS accelerators, *J. Instrum.* **15**, P07023 (2020).
- [18] L. Huang *et al.*, Longitudinal dynamics study and optimization in the beam commissioning of the rapid cycling synchrotron in the China Spallation Neutron Source, *Nucl. Instrum. Methods Phys. Res., Sect. A* **998**, 165204 (2021).
- [19] Y.-S. Yuan, N. Wang, S. Xu, and S. Wang, A code for the optimization of rf voltage waveform and longitudinal beam dynamics simulation in an RCS, *Nucl. Instrum. Methods Phys. Res., Sect. A* **729**, 864 (2013).